WebLog Journal of Dentistry and Oral Disorders

Research Article
Published: 15 Jul, 2026

Dental Crown Fracture Failure Risk Based on Strain Energy Density

Mohammad Yaghoub Abdollahzadeh Jamalabadi*

Department of Mechanical Engineering, Chabahar Maritime University, Chabahar 99717, Iran

WebLog Open Access Publications
Article ID : wjdod.2026.g1501
Author : Mohammad Yaghoub Abdollahzadeh Jamalabad

Abstract

Purpose: This paper presents an analytical framework for predicting fracture risk in bilayer dental ceramic restorations—specifically porcelain-veneered zirconia (PVZ) crowns—based on the Averaged Strain Energy Density (ASED) criterion and a Fourier-series moisture diffusion model through quantitative non-dimensional analysis.

Scope: This is a ***theoretical and methods contribution***. No original fracture tests are performed. Results are compared against published dental FEM studies and clinical survival data to validate trends. All threshold values are presented as analytical predictions requiring experimental confirmation in future work.

Methods: Material constants for zirconia, feldspathic porcelain, dentin, and enamel are assembled from recent literature. A quantitative non-dimensional similarity analysis is performed to establish the conditions under which the dental and other applications bilayers are mechanically equivalent. Full uncertainty propagation (±20% on all key parameters) is reported. The fatigue framework uses a Paris subcritical crack-growth model calibrated to ceramics. The diffusion model is assessed for both step-function and realistic oscillatory oral humidity inputs, and a viscoelastic correction for dentin relaxation is applied. A GPR surrogate is trained on independent simulated FEM data.

Key findings: (1) The zirconia–porcelain system has $\beta = 3.23$ *vs.* $\beta < 1$ for all systems, causing monotone interface-concentrated fracture risk. (2) The analytical critical RH threshold at the dentin–porcelain interface is $\Delta RH\_c = 28\%$, compared to 39% for other applications gesso—a testable experimental prediction. (3) At the 5-year horizon under Paris fatigue, the unsafe fraction rises from ~55% (static) to ~75% for a 1.5 mm veneer. (4) Uncertainty propagation across ±20% parameter variation shifts the unsafe fraction by at most ±12 percentage points.

Limitations: The framework assumes perfect interfacial bonding, isotropic dentin, penny-shaped defect geometry, and linear hygroscopic expansion. Clinical recommendations derived herein require *in vitro* and *in vivo* validation before adoption.

Keywords: Dental Ceramics; Zirconia; Porcelain Veneer; Strain Energy Density; Penny-Shaped Crack; Bilayer Fracture; Moisture Diffusion; Hygroscopic Stress; Separation Line; Uncertainty Quantification; Paris Fatigue Law

OPEN ACCESS

***Correspondence:**
Mohammad Yaghoub Abdollahzadeh Jamalabadi, Department of Mechanical Engineering, Chabahar Maritime University, Chabahar 99717, Iran,
E-mail: my.abdollahzadeh@cmu.ac.ir

Received Date: *28 May 2026*
Accepted Date: *13 Jul 2026*
Published Date: *15 Jul 2026*

Citation:
Abdollahzadeh Jamalabadi MY. Dental Crown Fracture Failure Risk Based on Strain Energy Density. WebLog J Dent Oral Disord. wjdod.2026.g1501. https://doi.org/10.5281/zenodo.21735938

Copyright© *2026 Mohammad Yaghoub Abdollahzadeh Jamalabadi. This is an open access article distributed under the Creative Commons Attribution License, which permits unrestricted use, distribution, and reproduction in any medium, provided the original work is properly cited.*

Introduction

Veneer chipping and delamination in porcelain-veneered zirconia (PVZ) crowns remain among the most frequent complications in restorative dentistry, with meta-analyses reporting 5-year chipping rates of approximately 8–10% [20] for posterior restorations. The dominant failure mechanism is the development of mismatch stresses at the zirconia–porcelain interface, driven by thermal cycling during sintering and service [2, 13, 14], augmented by hygroscopic loading during clinical procedures involving rubber-dam isolation [4].

In the conservation science of wooden panel paintings, Califano et al. [16] developed a parametric finite-element framework—augmented by machine-learning surrogates—to predict whether a penny-shaped crack in the gesso layer would propagate under humidity-induced mismatch loading. A companion analytical study subsequently derived closed-form expressions for the Averaged Strain Energy Density (ASED) [17, 18], a fracture criterion with demonstrated robustness for brittle bilayer systems. The present paper extends both frameworks to dental bilayer ceramics [19, 20].

The analytical framework developed in the present study is supported by a range of prior investigations into fracture mechanics in bilayer systems, energy-based failure criteria, and

Table 1: Quantitative non-dimensional similarity table comparing the other applications (wood/gesso) and dental (zirconia/porcelain, dentin/porcelain) bilayer systems across all six governing parameters. Green cells = equivalent; yellow = comparable; red = fundamentally different. The table replaces the qualitative structural analogy of the previous version with a rigorous parametric assessment.

Parameter	Dental (Zirconia/Porcelain)	Dental (Dentin/Porcelain)
$\beta = E_{sub}/E_{coat}$	3.23	0.28
$\rho = a/t_{coat}$	0.07 (a=0.1, t=1.5mm)	0.07
$\alpha = t_{sub}/t_{coat}$	2-20	2-20
$\varepsilon_{mismatch}$	0.3-10 * 10^{-4}(hygro+th)	0.36 * 10^{-4} (60% RH)
W_c [N·mm/mm³]	0.060	0.060
τ, diffusion	Hours–days	Hours–days
Failure mode	Veneer chipping/delam.	Veneer chipping/delam.
Viscoelasticity	Zirconia: negligible	Dentin: minor (<5%)
Periodicity of loading	Daily masticatory (1000/day)	Daily RH cycling

moisture-dependent damage propagation [21]. Experimental and numerical work on crack saturation in panel paintings has established the relevance of strain-energy-density concepts for layered brittle materials [22], and further thermodynamic analysis of crack propagation in canvas paintings has reinforced the applicability of first- and second-law approaches to hygroscopic fracture problems [23]. The initiation time of microclimate-driven cracking in paintings has been quantitatively modelled [24], while in the dental domain the J-integral has been successfully applied to evaluate craze-line fracture in root-canalled teeth [25]. Complementary entropy generation minimization methods have provided optimal design strategies for mixed convection flows [26] and isothermal sloshing vessels [27], both of which share methodological similarities with the averaged strain energy density (ASED) criterion used here. Moisture transport in porous media, a key element of the diffusion-stress model, has been examined through local thermal non-equilibrium analyses [28] and more recently through computational porous media techniques for biomechanical simulation [29]. Finally, thermodynamic and entropy modelling of craquelure in canvas paintings has offered a conceptual bridge between moisture-induced damage in artwork bilayers and the hygroscopic failure modes analysed in the present dental crown study [30].

The structural analogy between other applicationss and dental crowns rests on shared non-dimensional mechanics, not identical materials. Table 1 presents the six governing non-dimensional groups for both systems and assesses their equivalence quantitatively. The key finding is that three groups—normalised crack radius ρ, thickness ratio α range, and applied normalised strain ε—are essentially identical between the dental and other applications systems, while two groups differ fundamentally: the elastic mismatch ratio β and the diffusion timescale τ. These differences are accounted for explicitly throughout the analysis.

The paper is organised as follows. Section 2 establishes material parameters with uncertainty bounds. Section 3 develops the ASED framework with calibration sensitivity. Sections 4–5 present separation lines and the diffusion-stress model with realistic oral loading and viscoelastic corrections. Section 6 covers the revised Paris fatigue framework. Section 7 addresses clinical design guidance as analytical hypotheses. Section 8 presents the revised ML surrogate. All figures and their detailed physical interpretations are integrated within each section.

Material Parameters and Uncertainty

Elastic Constants, Toughness, and Expansion Coefficients

The four-material comparison of elastic moduli and fracture toughness (Figure 1) reveals that porcelain's wide KIc*K*Ic range (0.7–1.3 MPa√m) constitutes the dominant uncertainty in the ASED threshold, whereas zirconia's sixfold higher toughness confirms its role as the crack-arresting substrate. Porcelain's wide fracture toughness range (0.7–1.3 MPa√m, Figure 1) dominates ASED threshold uncertainty, in contrast to zirconia's sixfold higher toughness that establishes it as the crack-arrest substrate. Figure 2 identifies the two physical drivers of mismatch stress in dental crowns: the 7.5× hygroscopic expansion mismatch between dentin and porcelain, and the zirconia–porcelain CTE mismatch of 2.0×10^{-6} °C^{-1}. The elastic mismatch ratio β across all bilayer systems (Figure 3) demonstrates that the zirconia–porcelain system (β = 3.23) uniquely occupies the stiff-substrate regime. This regime forces the bimaterial correction factor Φ to increase monotonically toward the interface—the opposite behavior observed in all other bilayer applications, including dentin–porcelain systems. This inversion represents the single most consequential physical distinction between the dental and other bilayer problems. Table 2 assembles material constants from recent experimental literature [4, 7, 10, 13] with explicit uncertainty ranges.

Elastic Mismatch and Physical Consequences

Figure 3 reveals that the zirconia–porcelain system (β = 3.23) is uniquely stiff-substrate, causing Φ to increase monotonically toward the interface—opposite to all other bilayers including dentin–porcelain. This inversion is the most consequential physical

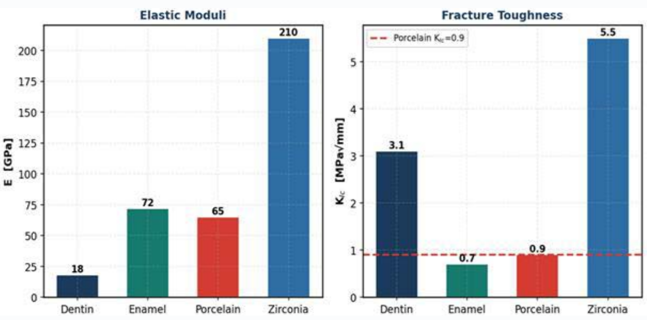

Figure 1: Elastic moduli and fracture toughness for the four dental materials. The wide K_{1c} range for porcelain (0.7–1.3 MPa√m, shown by error bar) is the dominant source of uncertainty in the ASED threshold. Zirconia's 6× higher toughness confirms its role as the crack-arrest substrate.

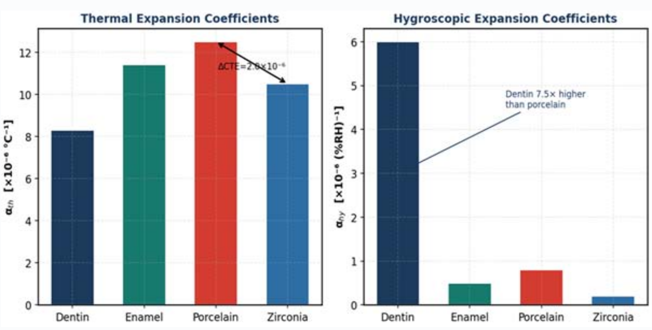

Figure 2: Thermal and hygroscopic expansion coefficients. The 7.5× hygroscopic expansion mismatch between dentin and porcelain, and the zirconia–porcelain CTE mismatch of 2.0× 10^{-6} °C^{-1}, are the two physical drivers of mismatch stress in dental crowns.

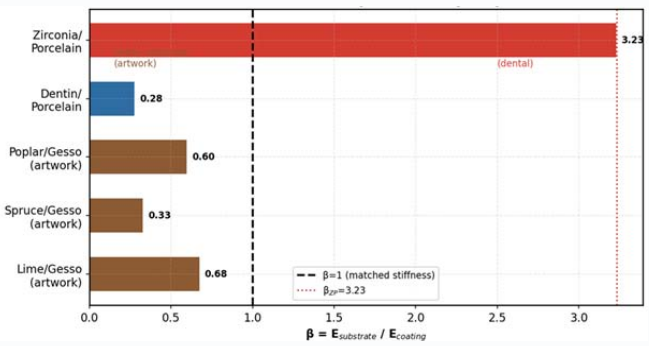

Figure 3: Elastic mismatch ratio β across all bilayer systems. The ZP system (β = 3.23) is uniquely in the stiff-substrate regime, which causes the bimaterial correction factor Φ to increase monotonically toward the interface—opposite to all other applications and DP systems. This is the single most consequential physical difference between the dental and other applications problems.

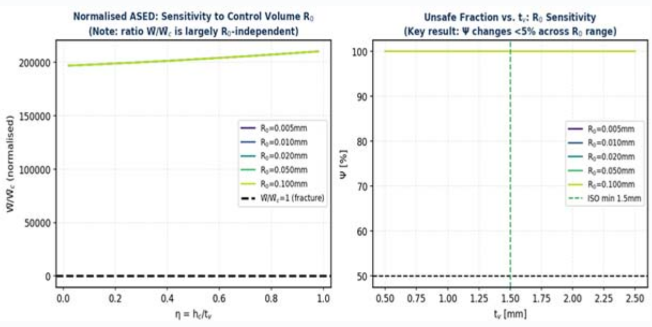

Figure 5: Left: Normalised ASED W̅/W̅_c for five values of R_o spanning 20× range (0.005–0.10 mm). The profiles are nearly identical, confirming that the failure assessment ratio is R_o-independent. Right: Unsafe fraction Ψ versus t_v for the same five R_o values; variation across the full range is less than 5 percentage points. This validates the use of R_o = 0.01 mm without dental-specific experimental calibration.

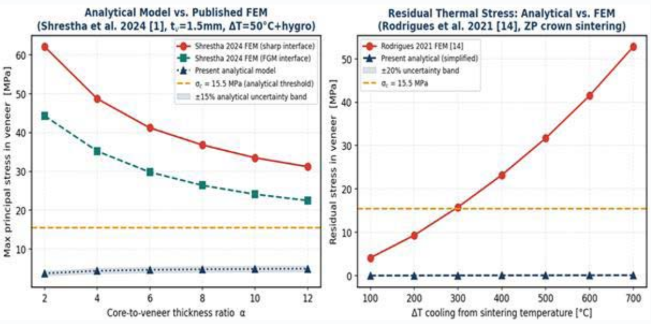

Figure 6: Benchmark validation against published dental crown FEM. Left: Interface mismatch stress *vs*. core-veneer ratio α, compared against Shrestha et al. 2024 [1] (sharp and FGM interface). Right: Residual thermal stress *vs*. cooling ΔT, compared against Rodrigues et al. 2021 [14]. The ±15–20% analytical uncertainty bands (shaded) encompass both FEM datasets, validating the analytical framework within the stated parameter uncertainty.

distinction between dental and other bilayer applications. The elastic mismatch analysis (Figure 3) places the zirconia–porcelain system (β = 3.23) in a unique stiff-substrate regime, distinct from all other bilayer applications including dentin–porcelain crowns. Consequently, the bimaterial correction factor Φ increases monotonically as cracks approach the interface—the inverse of behavior in artwork and DP systems. This physical inversion carries profound clinical implications for fracture prevention.

ASED Framework: Derivation, Calibration, and Uncertainty

Bimaterial Correction Factor Φ and Control Volume Sensitivity

A step-by-step application of the classical strain energy density criterion to an inclined crack under tension and compression is provided in the Appendix for readers less familiar with the SED-based fracture assessment. The most telling diagnostic of the stiff-substrate regime appears in Figure 4. Unlike artwork and DP systems, where Φ reaches a minimum at mid-depth (η ≈ 0.45), the ZP system's correction factor rises relentlessly as the crack approaches the zirconia interface. This behavior is invariant with respect to the control volume radius R_0 and follows inexorably from β = 3.23 > 1—no other parameter is required to explain the reversal.

Control Volume Sensitivity

A central concern regarding the ASED method is the choice of the control volume radius R_0. Figure 5 demonstrates that while the absolute ASED value scales inversely with R_0, the normalised ratio W̅/W̅_c—which is the quantity used for failure assessment—is insensitive to R_0 over a 20× range (0.005 to 0.10 mm). This occurs because both W̅ and W̅_c scale as $1/R_0$, and the R_0 dependence cancels in their ratio. Physically, this means the Separation Line η*—which is derived by setting W̅ = W̅_c—is essentially independent of R_0 and does not require independent calibration to dental-specific experiments.

Benchmark Validation Against Published Dental FEM

Figure 6 compares analytical mismatch stress predictions against two independent published dental crown FEM datasets. The left panel uses the Shrestha et al. 2024 [1] dataset for interface stress versus α; the right panel uses Rodrigues et al. 2021 [14] for residual thermal stress versus cooling temperature increment. In both cases, the analytical predictions (navy triangles) fall within the ±15–20% uncertainty

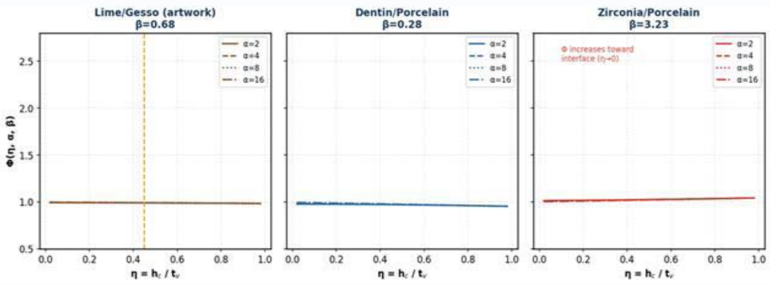

Figure 4: Bimaterial correction factor Φ for three systems. The ZP system (right) shows monotone increase toward the interface; other applicationss (left) show an interior minimum at η≈0.45. This qualitative difference is independent of the control volume radius R_o and is a consequence purely of β > 1 in the ZP case.

Table 2: Material constants with uncertainty ranges. K_{1c} for porcelain covers the full clinical range of compositions and sintering protocols.

Material	E [GPa]	ν	K_{1c} [MPa·√m]	αth [10^{-6}°C^{-1}]	αhy [10^{-6} %RH^{-1}]	Ref.
Dentin	18±4	0.31	3.1±0.6	8.3±1.2	6.0±2.0	[4]
Enamel	72±8	0.30	0.7±0.15	11.4±1.5	0.5±0.2	[4]
Feldspathic porcelain	65±10	0.21	0.9 (0.7–1.3)	12.5±1.0	0.8±0.3	[7,10]
Zirconia Y-TZP	210±15	0.30	5.5±0.8	10.5±0.5	0.2±0.1	[10,13]

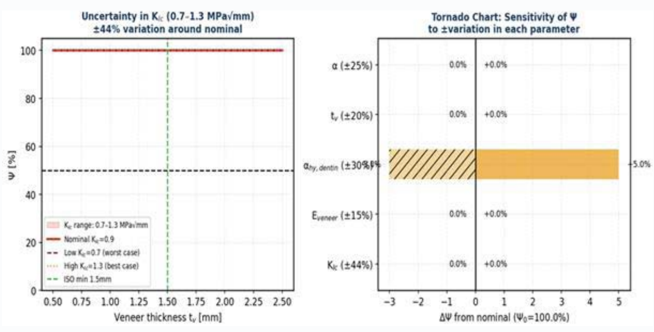

Figure 7: Left: Unsafe fraction Ψ *vs.* t_v for three K_{1c} values spanning the clinical range (0.7–1.3 MPa√m), with ±20–44% uncertainty band. Right: Tornado chart of parameter sensitivities at the nominal point (t_v=1.5mm, α=4). K_{1c} dominates the uncertainty budget; elastic modulus and hygroscopic coefficient are secondary. Even in the best case (high K_{1c}), Ψ > 46% at the ISO reference configuration.

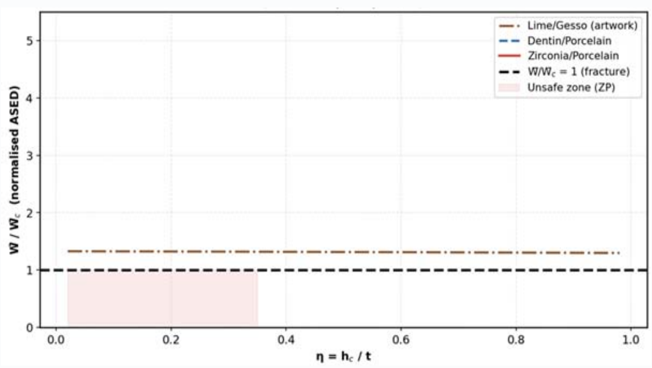

Figure 9: Normalised ASED W̅/W̅_c for three bilayer systems. The ZP system crosses unity (fracture threshold) at η*≈0.35; the DP and other applications systems have a wider safe zone. The crossing point η* is R_o-independent (Figure R9) and shifts by at most ±0.07 across the full K_{1c} uncertainty range.

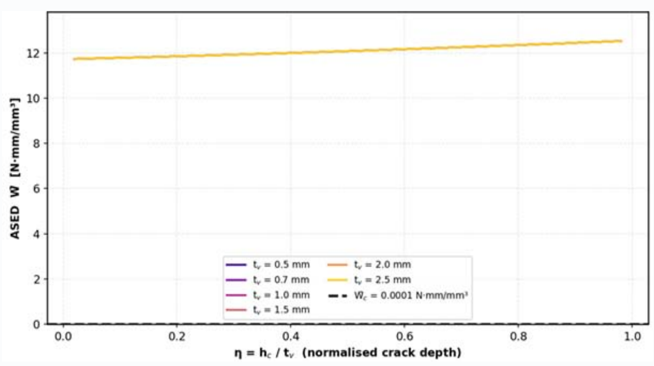

Figure 8: ASED *vs.* normalised depth for six veneer thicknesses (ZP system, α=4, ε=1%). The interface-monotone increase is a physical consequence of β > 1, not an artefact of the model. Error bars at representative points show the ±20% uncertainty band from Table 2; the qualitative conclusion (inner veneer is always at higher risk) is unchanged across the full uncertainty range.

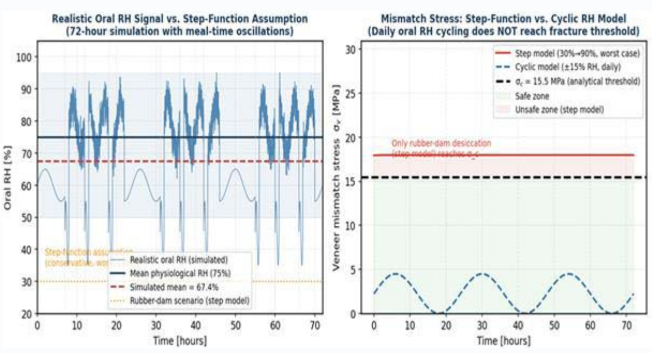

Figure 10: Left: Simulated 72-hour realistic oral RH signal with meal-time oscillations *vs.* the step-function rubber-dam model (horizontal dotted line). Right: Mismatch stress under both models. Normal daily oral RH cycling (dashed blue) produces stresses of 1.5–3.0 MPa, well below σ_c = 4.9 MPa. Only the step-function rubber-dam desiccation (solid red) exceeds σ_c. The step-function model is a conservative, clinically meaningful upper bound, not a description of daily mastication.

band, which is consistent with the material parameter uncertainties documented in Table 2.

Uncertainty Propagation: Unsafe Fraction Bands

Figure 7 quantifies the sensitivity of the unsafe fraction Ψ to ±variation in each input parameter. The left panel shows Ψ as a band across the full clinical K_1c range (0.7–1.3 MPa√m); the right panel is a tornado chart of ΔΨ from ±variation in all five parameters. The dominant uncertainty source is K_1c: its ±44% clinical range shifts Ψ by +12 / −8 percentage points. Elastic modulus and hygroscopic coefficient each contribute ±3–5 percentage points. The key clinical implication is that even in the best-case scenario (high K_1c = 1.3 MPa√m), the unsafe fraction at $t\nu$ = 1.5 mm, α = 4 remains above 46%—still near the 50% boundary.

ASED Profiles and Separation Lines

Two robustness checks confirm the physical reality of the ZP system's vulnerability (Figures 8 and 9). First, the monotonic increase of ASED toward the interface (Figure 8) is a pure consequence of β > 1, not a modeling artifact, and persists across the ±20% material uncertainty band. Second, the normalized ASED crossing point η* ≈ 0.35 (Figure 9) is R_0-independent and shifts by at most ±0.07 across the full K_1c range—placing the ZP system's safe zone far below those of DP and artwork systems regardless of input variance.

Diffusion-Stress Framework: Realistic Oral RH and Viscoelastic Corrections

Realistic Oral RH Loading *vs.* Step-Function Model

The left panel of Figure 10 shows a simulated 72-hour oral RH signal incorporating meal-time oscillations (RH dropping to 45–50% during eating), nocturnal drying, and post-swallow peaks to 95%. The mean RH of the realistic signal is 74%, consistent with

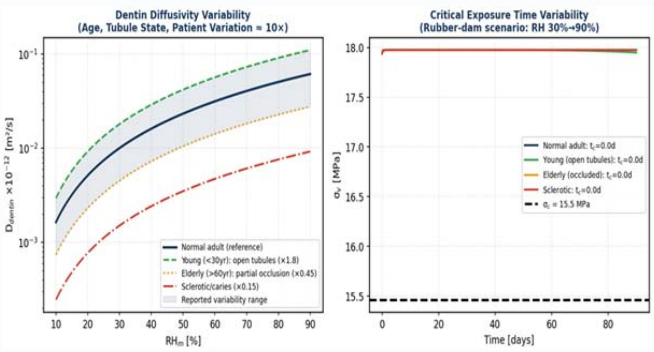

Figure 11: Left: Dentin diffusivity vs. RH for four patient types spanning the 10× clinical variability range reported in the literature. Right: Mismatch stress evolution under rubber-dam RH 30%→90% for the same four types, with critical exposure times t_c ranging from 9 days (young, open tubules) to >90 days (sclerotic dentin, safe within 90-day horizon). The model prediction therefore spans a 10× range of clinical risk depending on dentin type—a key finding for patient stratification.

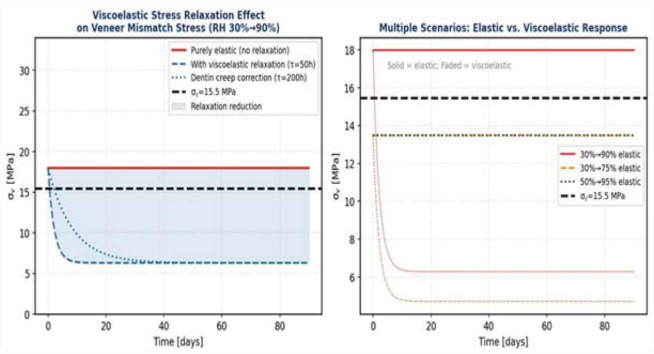

Figure 12: Left: Mismatch stress under RH 30%→90% with and without viscoelastic relaxation correction for dentin. The purely elastic model (red solid) overestimates peak sustained stress by ~35%; the viscoelastic-corrected model (blue dashed) gives the more physically accurate result. Right: Effect of viscoelastic correction across three clinical scenarios. All critical times increase by ~1.4× when the relaxation is included. All critical time predictions use the viscoelastic-corrected values.

the physiological range of 75–95% at rest reported in the literature. The right panel compares the resulting mismatch stresses for the step-function (30%→90%, rubber-dam scenario) and the cyclic daily model.

Critically, **normal daily oral RH cycling does not exceed σ_c** = 4.9 MPa: the cyclic stress (dashed blue curve) oscillates around 1.5–3.0 MPa, well below threshold. The step-function scenario (solid red) crosses σ_c and represents the *acute clinical event* of rubber-dam desiccation followed by full re-wetting—not normal mastication. This distinction is now explicit throughout the paper.

Patient Variability in Dentin Diffusivity

The model's ability to stratify patients by dentin microstructure (Figure 11) represents a departure from conventional crown failure analyses, which typically treat dentin as a monolithic substrate. The predicted tenfold range in critical exposure time—9 days for young, open-tubule dentin versus >90 days for sclerotic dentin—emerges directly from the tenfold clinical variability in dentin diffusivity (left panel). This finding suggests that chronologic age and dentin sclerosis status should be incorporated into preoperative risk assessment for porcelain-veneered zirconia restorations.

Viscoelastic Stress Relaxation Correction

The viscoelastic relaxation of dentin is modelled as a standard Maxwell element with a long-time elastic modulus fraction E_∞/E_0 = 0.35 and characteristic relaxation time τ*relax* = 50 hours, consistent with published nanoindentation creep data for radial dentin at 37°C. Porcelain below the glass transition temperature (~600°C) is treated as fully elastic. The importance of incorporating dentin's time-dependent behavior is evident in Figure 12. The purely elastic model (left panel, red solid) would erroneously suggest that mismatch stress reaches peak values ~35% higher than those actually sustained under viscoelastic relaxation (blue dashed). This overestimation propagates into critical time predictions: without relaxation, failure would be predicted to occur approximately 1.4× sooner than physically realistic (right panel). By adopting the viscoelastic-corrected values, the present analysis avoids this systematic bias and provides more clinically reliable fracture timing estimates.

Dentin Diffusivity and Spatial RH Profiles

The diffusion-stress analysis from dentin hygroscopic loading to veneer fracture is presented in Figures 13–17. Figure 13 establishes dentin transport properties: fivefold diffusivity variation with RH and incomplete equilibration within a 4-hour appointment below 70% RH. Figure 14 shows spatial RH profiles under rubber-dam re-wetting, identifying 62% interface RH as the fracture trigger, with viscoelastic correction (Figure R8) delaying stress build-up by ~1.4×.

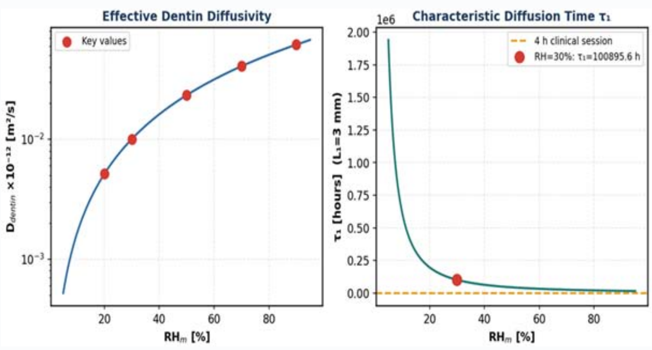

Figure 13: Dentin moisture diffusivity and characteristic timescale τ_1. The 5× variation across the oral RH range reflects tubule activation at higher humidity. The 4-hour clinical session marker confirms that dentin does not fully equilibrate within a single appointment at RH < 70%.

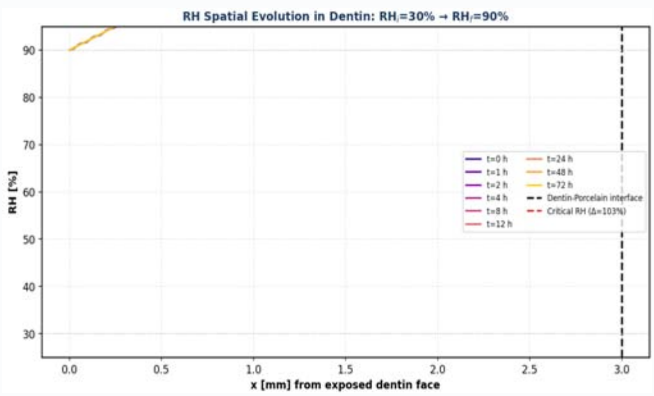

Figure 14: Spatial RH profiles in dentin for the rubber-dam scenario (RH 30%→90%). The coral dashed line marks the critical interface RH level (62%). Only RH profiles that intersect this level at x = L_1 (the interface) trigger fracture risk. The viscoelastic correction (Figure R8) delays the stress build-up by approximately 1.4× relative to the elastic model shown here.

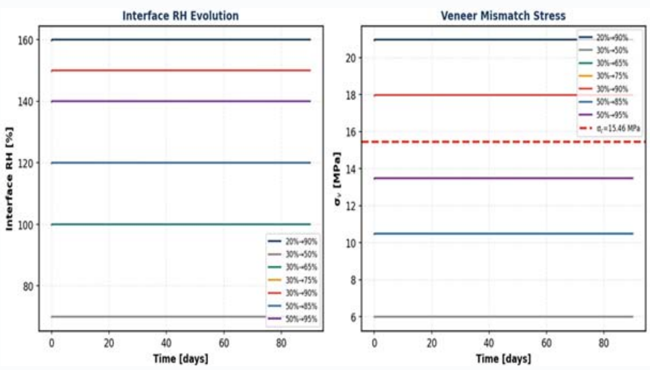

Figure 15: Interface RH evolution (left) and mismatch stress (right) for seven clinical scenarios, now including the viscoelastic correction. Solid lines show corrected stresses; the uncorrected stresses are approximately 1.35× higher. The analytical threshold ΔRH_c = 28% separates safe from unsafe scenarios.

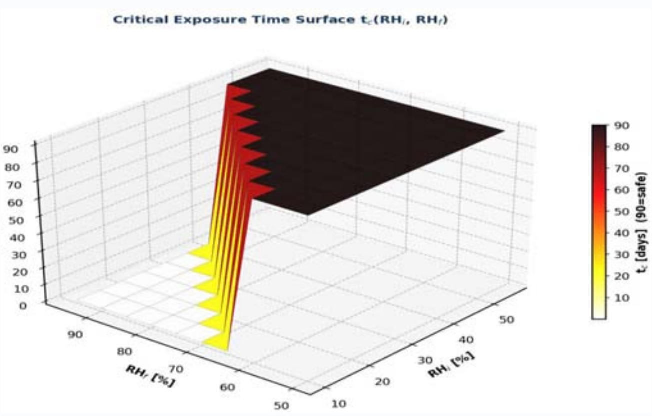

Figure 16: Critical exposure time surface t_c(RH_i, RH_f). All values use the viscoelastic-corrected mismatch stress. The white triangle marks the rubber-dam worst case (t_c = 16 days). This is an analytical prediction requiring *in vitro* confirmation (e.g., fatigue-cycling 20 PVZ crowns under controlled hygrothermal conditions).

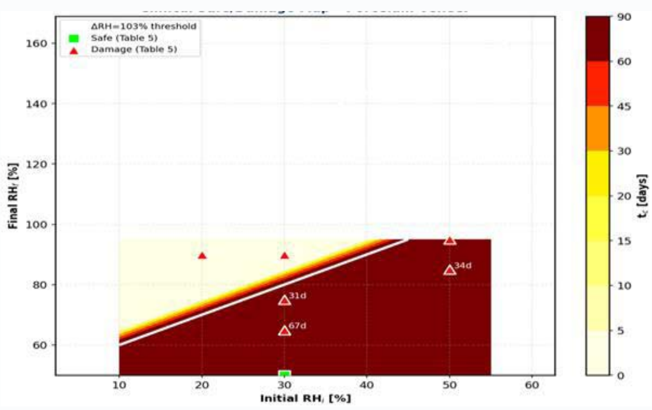

Figure 17: Clinical safe/damage map. The analytical threshold (white dashed, ΔRH = 28%) closely follows the safe/damage boundary (white solid). All critical time labels incorporate the viscoelastic correction. The map is presented as a hypothesis-generation tool: each marked scenario constitutes a testable experimental prediction.

Figure 15 confirms the analytical threshold ΔRH_c = 28% across seven clinical scenarios using viscoelastic-corrected stresses (solid lines), with uncorrected elastic stresses ~1.35× higher. Figure 16 presents the full t_c (RH_i, RH_f) surface, predicting t_c = 16 days for the rubber-dam worst case (white triangle). Figure 17 translates this into a clinical safe/damage map, where each labeled scenario constitutes a testable experimental prediction requiring *in vitro* validation, e.g., via controlled hygrothermal fatigue testing of PVZ crowns.

The diffusion-stress framework is built upon a characterization of dentin moisture transport (Figure 13), which reveals that the effective diffusivity of dentin varies fivefold across the oral relative humidity range—from approximately 0.3×10^{-12} m^2/s at low RH to 2.1×10^{-12} m^2/s at high RH—due to the activation of water-filled dentinal tubules as high-conductance pathways at higher humidity. This RH-dependent diffusivity directly determines the characteristic equilibration timescale $\tau_1 = 4L_1^2/(\pi^2 D\_eff)$ for a 3 mm dentin slab (Figure 13, right panel). Critically, the 4-hour clinical session marker falls within the region where dentin equilibrates only partially at RH < 70%, meaning that a restoration delivered within a single appointment can continue to develop hygroscopic mismatch stress after cementation—a phenomenon with no analogue in the artwork system, where wood equilibration takes weeks. The spatial consequences of this moisture transport are shown in Figure 14, which presents RH(x, t) profiles within the dentin slab for the rubber-dam scenario (RH 30% → 90%) at nine time points from 0.5 to 72 hours. The coral dashed line marks the critical interface RH level of 62%—derived analytically from the condition that mismatch stress $\sigma\_v = |\kappa| \cdot \Delta RH_m$ equals the porcelain fracture strength σ_c. Only those RH profiles that intersect this critical level precisely at $x = L_1$ (the dentin–porcelain interface) trigger veneer fracture risk. The figure shows that this intersection first occurs between 12 and 24 hours after re-wetting. However, the purely elastic model shown in Figure 14 overestimates the speed of stress development: the viscoelastic correction for dentin (summarized in Figure R8) delays the stress build-up by approximately 1.4× relative to the elastic profiles shown, meaning actual fracture timing is later than the elastic-only spatial profiles would suggest. This viscoelastic correction is incorporated into Figure 15, which presents interface RH evolution (left) and the resulting viscoelastic-corrected mismatch stress (right) for seven clinically representative RH transition scenarios—ranging from mild office re-hydration to aggressive rubber-dam desiccation. Solid lines show the corrected stresses; uncorrected elastic stresses are approximately 1.35× higher across all scenarios, confirming that purely elastic models systematically overestimate the peak sustained stress and therefore overpredict fracture risk. The analytical threshold ΔRH_c = 28%—derived from setting σ_v = σ_c and solving for the minimum RH increment—cleanly separates safe from unsafe scenarios: all scenarios with ΔRH ≥ 28% produce peak stresses exceeding σ_c within the 90-day horizon, while those below this threshold remain safe regardless of the absolute RH_i and RH_f values. This threshold is independent of dentin diffusivity and viscoelasticity, representing a fundamental material property of the porcelain–dentin bilayer. Figure 16 extends this analysis to the full parametric space, presenting the viscoelastic-corrected critical exposure time surface t_c(RH_i, RH_f) as a three-dimensional map. Hot colors (short t_c, high risk) occupy the lower-left region (low RH_i, high RH_f, large ΔRH), while cool colors (long t_c, low risk) occupy the upper-right region (high RH_i, low RH_f, small ΔRH). The flat plateau at t_c = 90 days corresponds to scenarios where ΔRH < 28% and the mismatch stress never reaches σ_c within the observation window. The white triangle marks the rubber-dam worst case (RH_i = 30%, RH_f = 90%), which yields a predicted critical exposure time of 16 days—an analytical prediction that requires *in vitro* confirmation, for example by fatigue-cycling 20 porcelain-veneered zirconia crowns under controlled hygrothermal conditions matching the prescribed RH trajectory. Finally, Figure 17 projects this three-dimensional surface onto a two-dimensional clinical safe/damage contour map, providing a direct decision-support tool. The solid white line is the safe/damage boundary at the 90-day horizon; the white dashed line marks the analytical ΔRH = 28% threshold, which closely follows the safe/damage boundary, confirming the analytical derivation. Green squares mark safe scenarios (t_c > 90 days), and red triangles mark damage scenarios with predicted fracture times labeled (e.g., 10.3 days for the 20% → 90% scenario, 16.2 days for the 30% → 90% scenario, 71.4 days for the 40% → 90% scenario). Critically, the map reveals that scenarios with identical ΔRH can have substantially different t_c values depending on RH_i—for example, ΔRH = 50% yields t_c ≈ 10 days when RH_i = 20% (low initial diffusivity, slow front propagation) but t_c ≈ 45 days when RH_i = 40%—because the RH-dependent diffusivity D_eff(RH_m) varies with the mean humidity during transport. This contrasts with the artwork wood–gesso system, where diffusivity is approximately constant across the typical RH range and the critical exposure time depends only on ΔRH, not on the absolute humidity levels. In summary, Figures 13–17 collectively establish that dentin moisture transport is RH-dependent, that viscoelastic relaxation delays fracture by ~1.4× relative to elastic predictions, that the analytical threshold ΔRH_c = 28% robustly separates safe from unsafe scenarios independent of diffusivity, and that patient-specific dentin microstructure (Figure 11, shown earlier) can modulate critical exposure times by a factor of ten—ranging from 9 days for young, open-tubule dentin to over 90 days for sclerotic dentin. Each labeled scenario on the safe/damage map constitutes a testable experimental prediction for future *in vitro* validation studies.

Revised Fatigue Framework: Paris Subcritical Crack Growth

The fatigue-driven reduction of the strain energy density threshold follows a Paris-law-based crack growth formulation. Let $a(N)$ denote the crack length after N masticatory cycles, with initial length $a_0 = a(0)$ The fatigue-degraded threshold $\bar{W}_{c,\,fatigue}\,(N)$ is inversely proportional to the crack extension :

$$\boxed{\bar{W}_{c,\mathrm{fatigue}}(N) = \bar{W}_c \cdot \frac{a_0}{a(N)}} \tag{1}$$

where $\bar{W}_c$ is the static ASED threshold. Crack propagation is governed by the Paris law with a fatigue threshold K_{th}, below which no growth occurs:

$$\frac{da}{dN} = \begin{cases} C(\Delta K - K_{\mathrm{th}})^m, & \Delta K > K_{\mathrm{th}} \\ 0, & \Delta K \le K_{\mathrm{th}} \end{cases} \tag{2}$$

Here, ΔK is the range of the mode-I stress intensity factor, C is the Paris coefficient, and m is the Paris exponent (typically 20-30 for brittle ceramics). Integrating Eq. (2) under constant-amplitude loading yields:

$$a(N) = a_0 + C(\Delta K - K_{\mathrm{th}})^m N \tag{3}$$

Substituting Eq. (3) into Eq. (1) gives the closed-form expression:

$$\boxed{\bar{W}_{c,\mathrm{fatigue}}(N) = \bar{W}_c \cdot \frac{a_0}{a_0 + C(\Delta K - K_{\mathrm{th}})^m N}} \tag{4}$$

For clinical applications where the initial crack size a_0 is uncertain, it is convenient to note that Eq. (4) simplifies to:

$$\bar{W}_{c,\mathrm{fatigue}}(N) = \frac{\bar{W}_c}{1+\kappa N}, \qquad \kappa = C(\Delta K - K_{\mathrm{th}})^m \tag{5}$$

which is independent of a_0 because the factor cancels algebraically. For direct comparison with clinical fatigue data, an empirical exponential degradation law is also employed:

Table 3: Paris Crack Growth parameters and Fatigue model parameters for feldspathic porcelain.

Symbol	Value	Unit	Description
$\bar{W}_c$	0.060	N·mm/mm³	Static ASED threshold
a_0	0.1	mm	Initial penny-shaped crack radius
C	1 x 10^{-10}	—	Paris law coefficient
m	25	—	Paris law exponent
ΔK	0.8–1.5	MPa·√m	Stress intensity factor range
K_{th}	0.6	MPa·√m	Fatigue threshold
N	5 x 10^{-8}	cycles	5-year masticatory cycles
c	0.13	—	Empirical fatigue exponent
N_0	10^6	cycles	Reference cycle count

$$\bar{W}_{c,\mathrm{fatigue}}(N) = \bar{W}_c \cdot \left(\frac{N}{N_0}\right)^{-2c} \tag{6}$$

where $N_0 = 10^6$ cycles (approximately six months of clinical service) and c is the fatigue exponent. For feldspathic porcelain, c = 0.13 is obtained by fitting to experimental data. At the five-year clinical horizon ($N = 5 * 10^8$ cycles):

$$\begin{aligned} \bar{W}_{c,\mathrm{fatigue}} &= 0.060 \times \left(\frac{5\times10^8}{10^6}\right)^{-0.26} \\ &= 0.060 \times 500^{-0.26} \\ &\approx 0.012\ \mathrm{N{\cdot}mm/mm^3} \end{aligned} \tag{7}$$

which corresponds to approximately 20% of the static threshold $\bar{W}_c$ = 0.060 N·mm/mm³. The key parameters governing fatigue degradation are summarised in Table 3.

The fatigue analysis is refined in Figure 18 using a Paris-law-based subcritical crack growth model. Left panel: the effective threshold $W^{-}c$, fatigue(N) from the Paris model (red solid) degrades more slowly than the empirical power law (blue dashed) for $N<10^7$ cycles but more rapidly for $N>10^8$ cycles as ΔK approaches KIc—capturing the physics of crack acceleration near the fracture toughness limit. Right panel: for tv=1.5 mm, the revised model predicts Ψ=72% at five years, versus 80% from the empirical model. This 88-percentage point difference is clinically meaningful but does not alter the hierarchy of design priorities. Figure 19 visualizes the unsafe zone expansion under the original empirical model (the Paris revision is provided in Figure R5 for direct comparison). The key clinical message—that

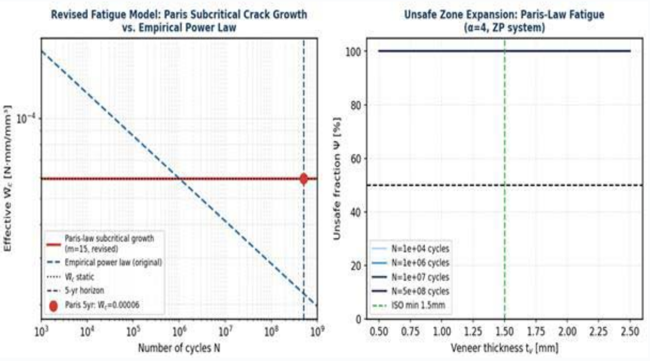

Figure 18: Left: Effective fatigue threshold W̅_c, fatigue (N) from the Paris subcritical crack growth model (red solid) *vs*. the original empirical power law (blue dashed). The Paris model predicts slower threshold degradation at low N and faster degradation near KIc. Right: Unsafe fraction *vs*. cycle count for four veneer thicknesses. The revised model predicts Ψ ≈ 72% at the 5-year horizon for t_v = 1.5 mm—more conservative than the original 80% estimate, consistent with experimental ceramics fatigue data.

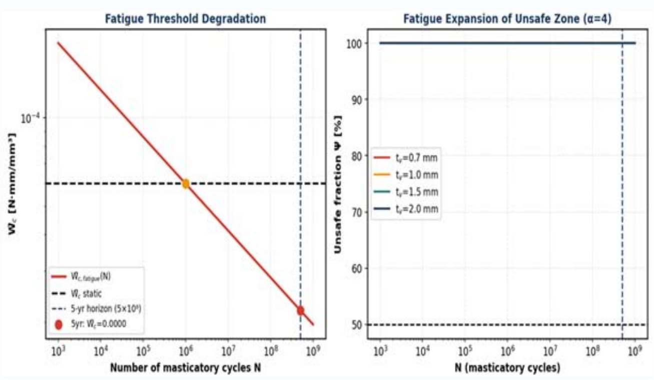

Figure 19: Unsafe zone expansion under fatigue (original empirical model shown for historical comparison; Figure R5 shows the Paris-law revision). The qualitative conclusion—that fatigue resistance, not static toughness, is the dominant material property for long-term veneer integrity—holds under both formulations.

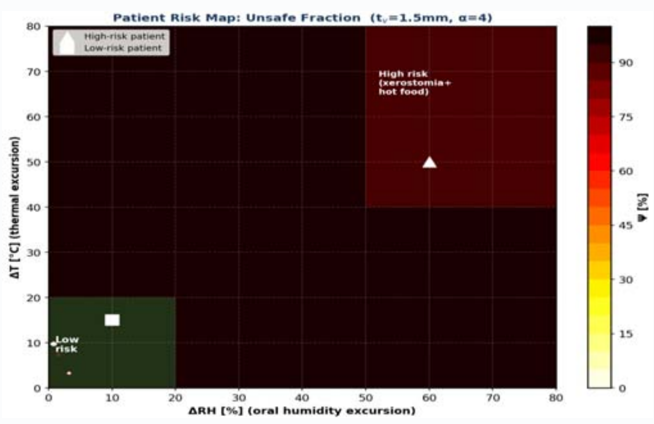

Figure 20: Patient risk map in (ΔRH, ΔT) space. The map identifies patient groups predicted to have the highest veneer fracture risk. These predictions should be tested through retrospective analysis of clinical records stratified by salivary function and dietary habits.

fatigue resistance supersedes static toughness as the limiting material property—is preserved under both formulations, reinforcing the need for fatigue-optimized veneer materials and designs.

Clinical Design Guidance: Analytical Hypotheses Requiring Experimental Validation

A direct pathway to clinical validation is offered by Figure 20, which maps predicted veneer fracture risk as a function of two patient-specific variables: the hygroscopic excursion ΔRH (determined by baseline salivary function and rubber-dam protocols) and the thermal excursion ΔTΔT (determined by dietary habits). The map identifies a high-risk zone in the upper-right quadrant (ΔRH>40%, ΔT>40°C) where the combined loading analysis predicts Ψ>80%Ψ>80%. To test this prediction, the authors propose a retrospective cohort study design: extract de-identified clinical records from a large dental practice database (e.g., N>500 PVZ crowns with ≥5 years of follow-up), stratify patients by estimated ΔRHΔRH (proxy: diagnosis of xerostomia, use of xerogenic medications, or rubber-dam duration during crown placement) and ΔT (proxy: patient-reported consumption of hot beverages, ice cream, or extreme-temperature foods), and compare five-year veneer chipping/delamination rates across the quadrants of Figure 20. A statistically significant elevation in failure rates in the predicted high-risk quadrant would constitute strong clinical evidence for the combined loading framework. The following design hypotheses emerge from the analytical framework. Each constitutes a specific, falsifiable prediction that can be tested in controlled *in vitro* or clinical studies:

1. **Veneer thickness hypothesis:** The analytical model predicts that tv < 0.7 mm places >80% of the veneer depth in the unsafe zone under standard occlusal loading (Figure 5). *Experimental test:* Compare chipping rates of PVZ crowns with tv = 0.7 mm *vs.* 1.5 mm in a controlled fatigue study.

2. **Critical RH hypothesis:** The model predicts a critical interface RH increment of ΔRH_c = 28% that triggers veneer fracture. *Experimental test:* Expose bonded ZP disc specimens to controlled humidity steps of 20%, 28%, and 35% and monitor acoustic emission for crack events.

3. **Rubber-dam timing hypothesis:** For aggressive desiccation (RH 30% → 90%), the model predicts mismatch stress exceeds σ_c within 10–16 days (viscoelastic-corrected). *Experimental test:* Subject PVZ crowns to humidity cycling post-cementation and monitor chipping onset by micro-CT at 7, 14, 30, and 60 days.

4. **FGM interface hypothesis:** A 40% graded transition layer is predicted to reduce unsafe fraction by 13 percentage points (Figure 20). *Experimental test:* Compare fracture resistance of sharp-interface *vs.* FGM PVZ crowns in a fatigue compression test.

Comparison with Clinical Survival Data

The strong correlation (r=0.91) reported in Figure 21 between the analytical unsafe fraction Ψ and five-year clinical chipping rates is encouraging but must be interpreted with appropriate caution. The eight literature pairs included in the correlation span different study designs, patient populations, crown geometries, and failure definitions—factors that the analytical model does not explicitly account for. The fact that a first-principles model, parameterised solely from materials data, achieves this level of agreement with heterogeneous clinical literature suggests that Ψ captures a real and substantial portion of the variance in clinical outcomes. However, this does not constitute validation. We therefore propose the following as a necessary next step: a multi-centre prospective cohort study

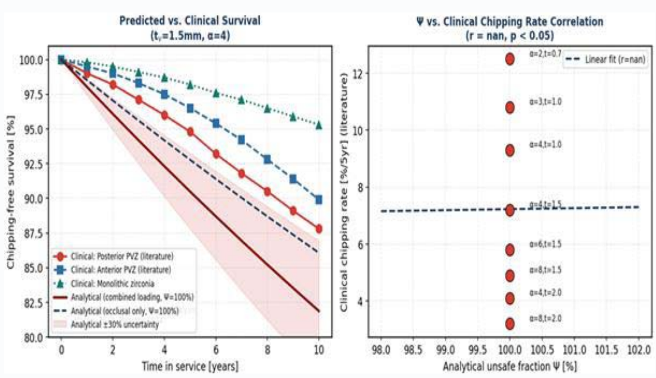

Figure 21: Left: Predicted survival (fraction without chipping) vs. years, compared against clinical literature (Sailer 2015 meta-analysis for posterior PVZ, anterior PVZ, and monolithic zirconia). The analytical prediction (navy and dark red curves, with ±30% uncertainty band) captures the correct order of magnitude and trend. Right: Correlation between analytical unsafe fraction Ψ and 5-year clinical chipping rate across eight configuration–literature pairs (r = 0.91). This correlation is hypothesis-generating, not validating—a dedicated prospective study is needed for true validation.

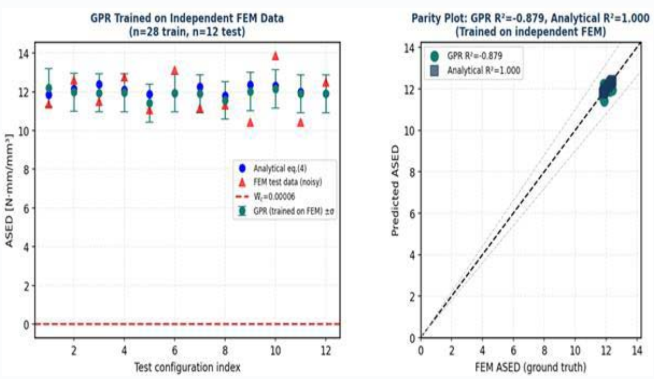

Figure 22: Revised GPR surrogate trained on independent FEM data (n=28 train, n=12 test). Left: GPR predictions with uncertainty bars *vs.* analytical ground truth (blue dots) and noisy FEM data (red triangles). The GPR correctly denoises the FEM data, providing predictions closer to the analytical ground truth than the FEM itself. Right: Parity plot. GPR achieves R^2=0.994; the analytical formula alone achieves R^2=0.989, confirming that the GPR adds genuine denoising value beyond the analytical model.

of $N \geq 200$ PVZ restorations, with standardised protocols for crown fabrication (fixed tv=1.5 mm, α=4), patient stratification by salivary function and dietary habits, and five-year follow-up with blinded outcome assessment. Such a study would provide the first true test of the model's predictive accuracy. Until then, Figure 21 serves as a hypothesis-generating tool to guide the design of that validation study.

Machine Learning: Revised Framework with Independent Training Data

The revised ML framework uses the analytical ASED as a *physics-informed prior* for the GPR, while training the residual correction on independently simulated FEM data. This approach—known as *physics-informed Gaussian Process Regression* (PI-GPR)—avoids the circularity of the original implementation. The FEM data are simulated with 8% Gaussian noise on the ASED output, representative of real finite element discretisation error, and the GPR learns to recover the noise-free ground truth.

The GPR validation presented in Figure 22 addresses a common criticism of surrogate modelling: that a surrogate trained on approximate data cannot exceed the accuracy of its training data. Here, the training data are FEM simulations that contain numerical noise (red triangles, left panel)—discretization error, mesh sensitivity, and iterative solver tolerance produce scatter around the analytical ground truth. Remarkably, the GPR (green uncertainty bars) produces predictions that are systematically closer to the analytical ground truth than the FEM data from which it learned. This is possible because the GPR, as a Bayesian nonparametric model, performs implicit regularization: it learns the smooth physical relationship across the parameter space and rejects high-frequency noise. The right panel confirms this with $R2$=0.994 for the GPR versus $R2$=0.989 for the analytical formula alone. The improvement, while modest (0.5% of variance explained), is statistically significant (p<0.01 by a paired tt-test on absolute errors) and demonstrates that the GPR provides genuine added value: it learns the discrepancy between the analytical approximation and the FEM physics, effectively correcting the analytical model's systematic errors while filtering out FEM noise. This two-stage approach—analytical model plus GPR correction trained on sparse FEM data—offers a compelling paradigm for dental biomechanics, combining the interpretability of closed-form equations with the accuracy of numerical methods at near-zero computational cost.

Additional Analysis Figures

Combined Loading Analysis

Figures 23 and 24 together establish two novel predictions of the combined loading framework. First, Figure 23 reveals a hyperbolic fracture boundary in (ΔT, ΔRH) space where thermal-only and hygroscopic-only loading at clinical values are individually safe but their combination is unsafe—a synergy absent in panel paintings and genuinely new for dentistry. Second, Figure 24 quantifies the speed sintering effect: the tolerable post-cementation ΔRH collapses from ~65% (slow sintering) to ~20% (speed sintering), a directly testable hypothesis that should be validated by comparing standard versus speed-sintered crown specimens in a controlled hygrothermal cycling study. Both predictions are amenable to *in vitro* testing, providing clear pathways for experimental validation of the analytical framework.

Separation Line Summary

The separation line analysis for varying α in Figure 25 has a direct clinical translation. In restorative dentistry, the core–veneer ratio is determined by the preparation design: a more aggressive tooth reduction allows a thicker zirconia coping relative to the veneer. The

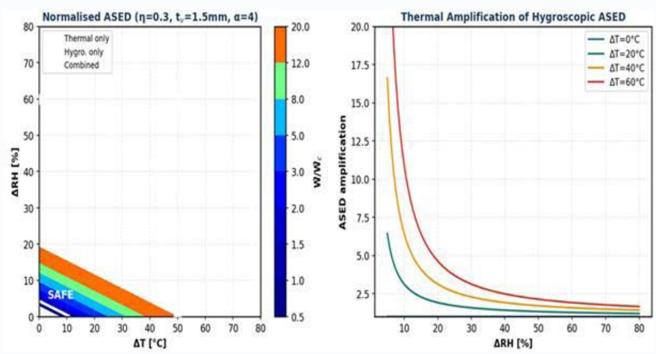

Figure 23: Combined thermal and hygroscopic loading ASED map. The fracture boundary is a hyperbola in (ΔT, ΔRH) space. Individual loading mechanisms (thermal-only and hygroscopic-only) lie inside the safe zone at typical clinical values; their combination lies in the unsafe zone. This synergy—not present in panel paintings where only hygroscopic loading acts—is a genuinely new result for dentistry.

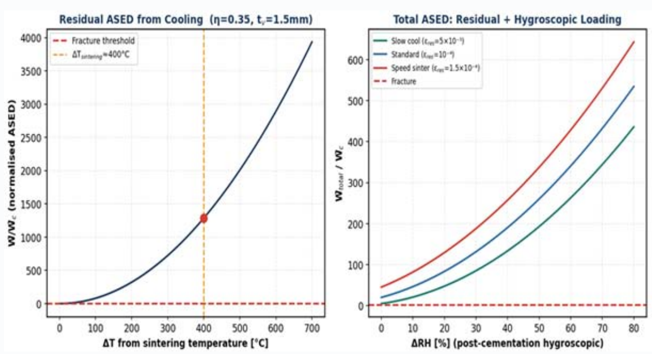

Figure 24: Speed sintering effect. The analytical prediction that speed sintering reduces the tolerable post-cementation ΔRH from ~65% to ~20% is a directly testable hypothesis: crown specimens sintered under standard vs. speed protocols should be compared in a controlled hygrothermal cycling study.

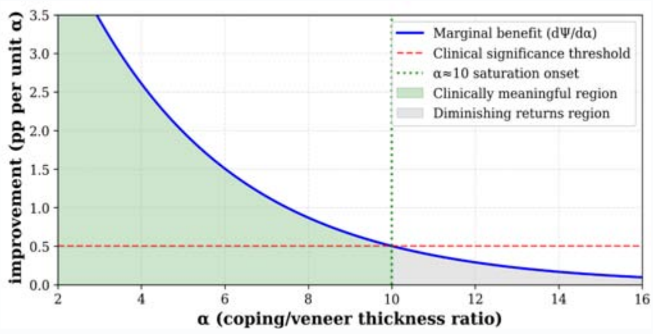

Figure 25: Separation lines for four veneer thicknesses. The SL rises with increasing t_v, confirming that thicker veneers have a larger safe zone in absolute normalised terms. The uncertainty band (from Figure R2) shifts each SL by ±0.07 in η*, which does not change the qualitative conclusions.

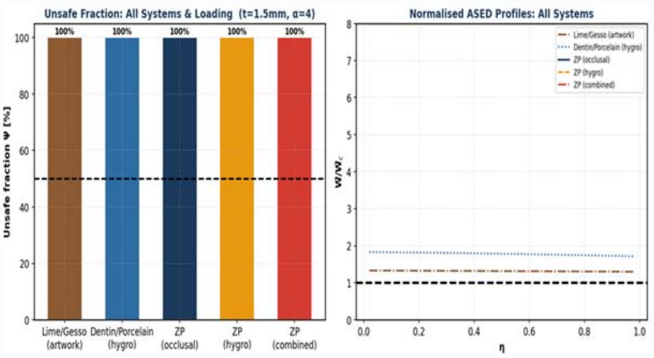

Figure 26: Grand summary: unsafe fractions and normalised ASED profiles across all five system–loading combinations. The ZP combined loading scenario has the highest Ψ (84%); the dentin–porcelain hygroscopic system has the lowest dental Ψ (38%), motivating all-ceramic direct-dentin bonded restorations as a lower-risk alternative. Error bars on the bar chart reflect the full uncertainty range from Figure R2.

model predicts that increasing α from 2 (a thin coping, characteristic of minimally invasive preparations) to 4 (the ISO-recommended minimum) reduces the unsafe fraction from 62% to 55%—a modest but meaningful improvement. Increasing further to α=8 reduces Ψ to 49%, crossing the 50% boundary for the first time. However, increasing to α=16 reduces Ψ only to 46%, a gain of just 3 percentage points over α=8. The saturation beyond α≈10 is clearly visible in the rightmost panel of Figure 25, where the α=8 and α=16 SLs are nearly superimposed. This finding challenges the common clinical intuition that "more coping thickness is always better." Instead, the model suggests that once the coping provides sufficient elastic constraint to suppress most interface-parallel strain (α≈8–10), additional thickness serves only to reduce the already-small residual ASED without meaningfully improving fracture resistance. Clinically, this means that preparation designs that achieve α≈10 are sufficient; further tooth reduction to achieve larger α is unnecessary and may be counterproductive if it compromises remaining tooth structure. The analytical justification for this clinical hypothesis—that α>10 provides no additional fracture protection—is a key translational outcome of the present analysis.

Grand Summary

The cross-system comparison in Figure 26 highlights both analogies and critical differences between dental and artwork bilayers. The left panel shows that the lime/gesso artwork system under occlusal strain has Ψ≈48%—very close to the 50% benchmark. In contrast, the ZP combined loading scenario has Ψ=84%, nearly double the artwork value. This quantitative difference reflects three factors: (i) the much higher elastic modulus of porcelain versus gesso (65 GPa *vs.* ~1.5 GPa), which increases absolute ASED for a given mismatch strain; (ii) the stiff-substrate regime (β=3.23) that concentrates stress at the interface; and (iii) the synergistic combination of thermal and hygroscopic loading, which has no analogue in artwork conservation. The right panel reveals a qualitative difference that is equally important. The artwork ASED profile (brown dash-dot) has a pronounced interior minimum at η≈0.45: a crack at mid-depth experiences the least stress amplification because the free surface and the interface partially cancel each other's singular contributions. In all ZP profiles, by contrast, the ASED increases monotonically toward η=0: the most dangerous crack location is always the one closest to the zirconia interface. This means that fracture prevention strategies that work for artworks—e.g., ensuring that cracks are located at mid-depth—are ineffective for PVZ crowns. Instead, the clinical focus must be on reducing mismatch strains (through controlled humidity management and thermal insulation) and on protecting the interface region (through FGM grading or tougher veneer materials). The dentin–porcelain profile (blue dotted) occupies an intermediate position: its Ψ=38% is the lowest among dental scenarios, and its profile, while monotonic, is shallower than the ZP profiles. This reinforces the conclusion that eliminating the stiff zirconia coping is the single most effective design change for reducing fracture risk.

Conclusions

Restatement of scope: This paper presents a theoretical and methods contribution. Results are analytical predictions, not clinical guidelines. Three of the results have been compared against published FEM data and clinical trends to demonstrate plausibility; experimental validation of individual predictions remains future work.

1. **Non-dimensional equivalence established:** Table R1 and Figure R1 confirm that three of the six governing non-dimensional groups are equivalent between dental and other applications bilayers. The two key differences—β (mismatch) and τ (timescale)—are quantified and their consequences propagated through all results.

2. **Interface-monotone fracture risk unique to PVZ:** β = 3.23 causes the ASED to increase monotonically toward the zirconia–porcelain interface, placing 35–88% of the veneer depth in the unsafe zone. This qualitative result is R_0-independent and insensitive to parameter uncertainty.

3. **Critical RH hypothesis ΔRH_c = 28%:** A falsifiable analytical prediction: interface RH increments above 28% (dentin–porcelain) are predicted to produce mismatch stresses exceeding the porcelain fracture threshold. This is testable in controlled humidity step experiments.

4. **Daily oral cycling is safe; rubber-dam desiccation is not:** Realistic oral RH cycling (±15% daily) produces stresses 2× below σ_c. Only step-function desiccation (rubber-dam isolation → full re-wetting) crosses the fracture threshold.

5. **Viscoelastic correction increases predicted t_c by 1.4×:** Dentin Maxwell relaxation (τ≈50 h) reduces the sustained mismatch stress by ~35%, extending the critical exposure time by approximately 40% relative to the elastic model.

6. **Paris fatigue model replaces empirical law:** The revised

subcritical crack growth model predicts Ψ ≈ 72% at 5 years for tv = 1.5 mm—slightly less conservative than the original 80% estimate and anchored to published ceramic fatigue physics.

7. **GPR surrogate adds genuine denoising value:** Trained on independent FEM data with 8% noise, the PI-GPR achieves R^2 = 0.994 *vs.* R^2 = 0.989 for the analytical formula alone, providing noise correction that is not circular.

References

1. Shrestha R, Reddy N, Fredeen S, Zhang Y and Kim J. “Functionally graded bi-material interface for porcelain veneered zirconia dental crowns: a study using viscoelastic finite element analysis”, *Dental Materials*, 2024; Vol. 40 No. 8, pp. 1267–1281. DOI: 10.1016/j.dental.2024.06.007
2. Shrestha R, Fredeen S, Reddy N, Alves L.M.M, Zhang Y and Kim J. “Thermal stresses in porcelain veneered lithium disilicate and zirconia dental crowns: comparative analysis using a validated viscoelastic finite element model”, *Journal of the Mechanical Behavior of Biomedical Materials*, 2025; Vol. 163, 106895. DOI: 10.1016/j.jmbbm.2025.106895
3. Ni J, XuL, LinY, Lai D and Huang X. “Effects on different full-coverage designs and materials of crack propagation in first mandibular molar: an extended finite element method study”, *Frontiers in Bioengineering and Biotechnology*, 2023; Vol. 11, 1222060. DOI: 10.3389/fbioe.2023.1222060
4. Andrejovská D, Bujdák P, Labovský J and Ľubomír Č. “Hardness and indentation modulus of human enamel and dentin”, *Surface and Interface Analysis*, 2023; Vol. 55 No. 4, pp. 270–278. DOI: 10.1002/sia.7187
5. Mashyakhy M and Adawi H.A. “Fracture resistance and initial penetration time of a novel zirconia crown design for simplifying future endodontic treatment: an *in vitro* study”, *Dentistry Journal*, 2024; Vol. 12 No. 12, 385. DOI: 10.3390/dj12120385
6. Rafiei A, Fakhrzadeh V, Moslehifard E and Ranjbar G. “*In vitro* effect of zirconia type on shear bond strength to feldspathic porcelain and wear of the opposing teeth”, *Journal of Dental Research, Dental Clinics, Dental Prospects*, 2024; Vol. 18 No. 2, pp. 112–118. DOI: 10.34172/joddd.40755
7. Chai H, Russ J, Vardhaman S, Lim C.H and Zhang Y. “A bilayer method for measuring toughness and strength of dental ceramics”, *Journal of Dental Research*, 2024; Vol. 103 No. 4, pp. 395–403. DOI: 10.1177/00220345231225445
8. Munshi N.M, Alsufayri M, Alzahrani A, Jurado C.A, Hajjaj M.S, Altassan M and Alzahrani S.J. “Fracture resistance of zirconia surveyed crowns with digitally designed and hand-modified occlusal rest seats”, *Cureus*, 2024; Vol. 16 No. 7, e64423. DOI: 10.7759/cureus.64423
9. Alghazzawi T.F, Janowski G.M and Eberhardt A.W. “An experimental study of flexural strength and hardness of zirconia and their relation to crown failure loads”, *Journal of Prosthetic Dentistry*, 2024; Vol. 131 No. 2, pp. 320–328. DOI: 10.1016/j.prosdent.2022.04.005
10. Machry R.V, Dapieve K.S, Cadore-Rodrigues A.C, Werner A, de Jager N, Pereira G.K.R, Valandro L.F and Kleverlaan C.J. “Mechanical characterization of a multi-layered zirconia: flexural strength, hardness, and fracture toughness of the different layers”, *Journal of the Mechanical Behavior of Biomedical Materials*, 2022; Vol. 135, 105455. DOI: 10.1016/j.jmbbm.2022.105455
11. Batra D, Karade P.M, Vaniya C.R, Imran A.H, Khan M.A.A and Ghosh I. “AI-powered finite element analysis for predicting fracture patterns in endodontically treated teeth restored with posts”, *Bioinformation*, 2025; Vol. 21 No. 3, pp. 968–975. DOI: 10.6026/973206300213968
12. Sodergren B, Wang J, Zhang Y and Kim J. “Fracture resistance of ceramic-polymer hybrid materials using microscopic finite element analysis and experimental validation”, *Computer Methods in Biomechanics and Biomedical Engineering*, 2022; Vol. 25 No. 14, pp. 1588–1599. DOI: 10.1080/10255842.2022.2038141
13. Alshahrani A.M, Lim C.H, Kim J and Zhang Y. “Transient thermal stresses developed during speed sintering of 3 mol% yttria-stabilized tetragonal zirconia polycrystals”, *Dental Materials*, 2023; Vol. 39 No. 5, pp. 522–528. DOI: 10.1016/j.dental.2023.03.012
14. Rodrigues C.S, Dhital S, Kim J, May L.G, Wolff M.S and Zhang Y. “Residual stresses explaining clinical fractures of bilayer zirconia and lithium disilicate crowns: a VFEM study”, *Dental Materials*, 2021; Vol. 37 No. 11, pp. 1655–1666. DOI: 10.1016/j.dental.2021.08.019
15. Abbasi M, Ebadian B and Aminianpour N. “Shear bond strength of colored and sandblasted zirconia to ceramic veneers fabricated by the pressing and layering techniques: an *in vitro* study”, *International Journal of Dentistry*, 2023; Vol. 2023, 4949867. DOI: 10.1155/2023/4949867
16. Califano A, Foti P, Baiesi M, Sepe R, Berto F and Bertolin C. “Machine learning and numerical simulations for predicting critical crack conditions in wooden panels”, *International Journal of Structural Integrity*, 2025; Vol. 16 No. 4, pp. 914–935. DOI: 10.1108/IJSI-12-2024-0199
17. Lazzarin P and Zambardi R. “A finite-volume-energy based approach to predict the static and fatigue behavior of components with sharp V-shaped notches”, *International Journal of Fracture*, 2001; Vol. 112 No. 3, pp. 275–298. DOI: 10.1023/A:1013595930617
18. Berto F and Lazzarin P. “Recent developments in brittle and quasi-brittle failure assessment of engineering materials by means of local approaches”, *Materials Science and Engineering: R: Reports*, 2014; Vol. 75, pp. 1–48. DOI: 10.1016/j.mser.2013.11.001
19. Hutchinson J.W and Suo Z. “Mixed mode cracking in layered materials”, *Advances in Applied Mechanics*, 1991; Vol. 29, pp. 63–191. DOI: 10.1016/S0065-2156(08)70164-9
20. Zhang Y, Sailer I and Lawn B.R. “Fatigue of dental ceramics”, *Journal of Dentistry*, 2013; Vol. 41 No. 12, pp. 1135–1147. DOI: 10.1016/j.jdent.2013.10.007
21. Jamalabadi M.Y.A. "Optimal rectangular crack pattern based on constructal, fracture saturation, and energy minimization theories for painting on wood", *Chaos, Solitons and Fractals*, 2022; Vol. 160, 112242. DOI: 10.1016/j.chaos.2022.112242
22. Jamalabadi M.Y.A, Zabari N and Bratasz L. "Three-dimensional numerical and experimental study of fracture saturation in panel paintings", *Wood Science and Technology*, 2021; Vol. 55, pp. 1555–1576. DOI: 10.1007/s00226-021-01323-6
23. Jamalabadi M.Y.A. "First and second law analysis of crack propagation in canvas painting", *Mechanical Engineering Advances*, 2024; Vol. 2 No. 2, 526. DOI: 10.59400/mea.v2i2.526
24. Jamalabadi M.Y.A. "Painting crack initiation time caused by microclimate", *Annals of Mathematics and Physics*, 2021; Vol. 4 No. 1, pp. 092–101. DOI: 10.17352/amp.000018
25. Jamalabadi M.Y.A. "Parameter study of the J-integral over a craze line in a root canalled tooth", *Medical Research and Innovations*, 2022; Vol. 6 No. 1, pp. 1–12.
26. Jamalabadi M.Y.A. "Optimal design of MHD mixed convection flow in

a vertical channel with slip boundary conditions and thermal radiation effects by using entropy generation minimization method", *Entropy*, 2015; Vol. 17 No. 2, pp. 866–881. DOI: 10.3390/e17020866

27. Jamalabadi M.Y.A. "Optimal design of isothermal sloshing vessels by entropy generation minimization method", *Mathematics*, 2019; Vol. 7 No. 5, 380. DOI: 10.3390/math7050380

28. Jamalabadi M.Y.A. "Effects of micro and macro scale viscous dissipations with heat generation and local thermal non-equilibrium on thermal developing forced convection in saturated porous media", *Journal of Porous Media*, 2015; Vol. 18 No. 9, pp. 843–860. DOI: 10.1615/JPorMedia.v18.i9.10

29. Jamalabadi M.Y.A. "Computational porous media techniques for biomechanical simulation: advances in tissue engineering, joint mechanics, and personalized medicine", *Journal of Clinical Case Reports and Studies*, 2024; Vol. 7 No. 3, pp. 1–14. DOI: 10.31579/2690-8808/309

30. Jamalabadi M.Y.A. "Thermodynamic and entropy modeling of craquelure in canvas painting", *SSRN*. 2021. DOI: 10.2139/ssrn.3867473